Remote Sensing of Environment 135 (2013) 202–212

Contents lists available at SciVerse ScienceDirect

Remote Sensing of Environment

journal homepage: www.elsevier.com/locate/rse

Unattended processing of shipborne hyperspectral reflectance measurements

Stefan G.H. Simis *, John Olsson

Finnish Environment Institute SYKE, Marine Research Centre, Erik Palménin Aukio 1, 00560 Helsinki, Finland

ARTICLE INFO

Article history:
Received 6 June 2012
Received in revised form 14 February 2013
Accepted 4 April 2013
Available online 8 May 2013

Keywords:
Reflectance
Sky radiance
Hyperspectral
Case-2 water
Shipborne monitoring

ABSTRACT

Hyperspectral remote-sensing reflectance (R_{rs}) from above-surface (ir)radiance measurements is derived using a new, automated method that is suitable for use on moving platforms. The sensors are mounted on a rotating platform that compensates for changing solar and ship azimuth angles, optimizing the sensor azimuth for minimal contribution of sky radiance to measured water-leaving radiance. This sea-surface reflectance (ρ_s) lies in the order of 2.5–8% of sky radiance, and is determined through spectral optimization, minimizing the propagation of atmospheric absorption features to R_{rs}. Up to 15 of these gas absorption features are frequently recognized in (ir)radiance spectra under clear and overcast skies. R_{rs} was satisfactorily reproduced for a wide range of simulated Case 2 waters and clear sky conditions. A set of 13,784 in situ measurements collected with optimized viewing angles on the high-absorption, low-scattering Baltic Sea was collected in April and July 2010–2011. The processing procedure yielded a 22% retrieval rate of ρ_s for the field data. The shape of the subsurface irradiance reflectance measurements ($R(0^-)$) measured at anchor stations was well reproduced in above-surface R_{rs} in those cases where the algorithm converged on a solution for ρ_s, except under unstable or weak illumination conditions. Clear-sky conditions resulted in the best correspondence of R_{rs} and $R(0^-)$ and gave the highest (>50%) retrieval rates of ρ_s. Two indices, derived from the available sensor data, are given to describe illumination conditions, and are shown to predict the ability of the algorithm to retrieve R_{rs}.

1. Introduction

Reflectance or water color, measured from submerged (ir)radiance sensors, from poles, rafts, or ships, or from remote (air- or spaceborn) platforms, can be a cost-effective solution for monitoring water quality and aquatic biogeochemical processes. Spectral features in reflectance can be related to the concentrations and inherent optical properties of optically active water constituents (Gordon et al., 1975; Kirk, 1994; Morel, 1980; Preisendorfer, 1976; Tyler, 1960). Satellite-born sensors allow the interpretation of the reflectance properties of the oceans in terms of global biogeochemical cycles (Behrenfeld & Falkowski, 1997; Falkowski et al., 1998). In coastal waters, lakes, and estuaries, remote sensing algorithms for water quality parameters often need to be regionally tuned and validated to yield meaningful results. In these 'optically complex' waters *a priori* knowledge of the reflectance properties of the water body and transmission properties of the atmosphere can be a great asset, helping reduce uncertainties in remote sensing algorithms and atmospheric correction.

Hyperspectral reflectance can be measured from fixed offshore platforms (Zibordi et al., 2006, 2009), moored buoys, or ships, to aid data assimilation with remote sensors and to provide continuous observations under cloud cover. Ship-based installations provide some advantages over stationary platforms: they allow easy access in the home harbor which reduces operational cost, and the wider spatiotemporal coverage from ships compared to stationary platforms yields an attractive diversity in observations to compare against satellite data. However, ship-based systems also face significant platform-specific problems. Whereas stationary platforms allow quality control based on statistics over subsequent recordings, this is not strictly possible from moving platforms where the same water mass is less likely to be observed in consecutive measurements (commercial ferries easily travel at 20 kn ≈ 10 m s^{-1}). Further, in order to avoid sun glitter, spray, and ship shadows, close-range reflectance measurements have to be carried out at viewing zenith angle (θ_v) that projects away from the ship, and a viewing azimuth angle φ_v away from the solar azimuth (φ_s) that is sufficiently large to avoid sun glint (Fig. 1). Angles of $\theta_v = 40°$ and $\varphi_v > 90°$ (ideally 135°) are considered suitable (Hooker & Morel, 2003; Mobley, 1999; Mueller et al., 2003). Even under optimized viewing angles, however, sun and sky radiance reflected at the sea surface shows a theoretical variation in the order of 2–6% of the downwelling radiance with varying sea surface roughness (Cox and Munk, 1954a, 1954b; Mobley, 1999). This reflected sky radiance can be of similar magnitude as the upwelling radiance in clear and moderately turbid waters and therefore constitutes the main error source in R_{rs} calculations (Doxaran et al., 2004). To correct for the reflection of sky radiance at the water

* Corresponding author.
E-mail addresses: stefan.simis@environment.fi (S.G.H. Simis), john.olsson@environment.fi (J. Olsson).

0034-4257
http://dx.doi.org/10.1016/j.rse.2013.04.001

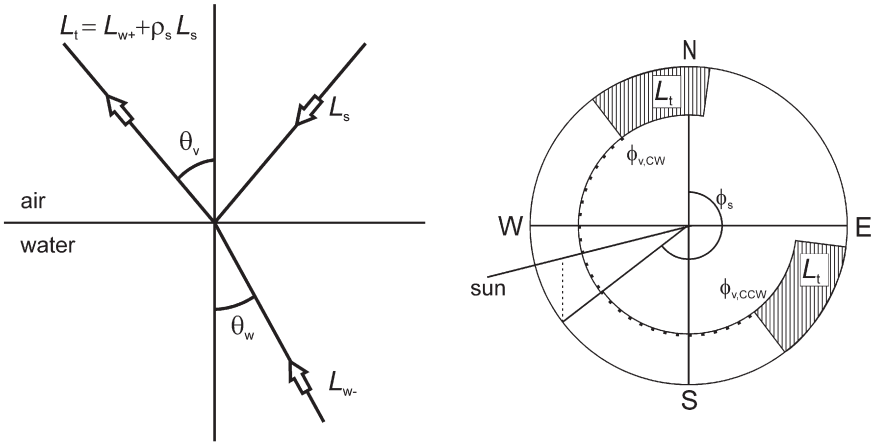

Fig. 1. Measurement geometry and used symbols in close-range remote sensing reflectance measurements (Eqs. 1a and 1b). The shaded areas in the second diagram indicate the angles under which L_t should be obtained ($90 \le \varphi_v \le 135°$ from solar azimuth φ_s).

surface, the following expression for close-range (above-surface) remote sensing reflectance is used:

$$R_{rs}(\lambda) = L_{w+}(\lambda)/E_d(\lambda) \quad (1a)$$

$$L_{w+}(\lambda) = L_t(\lambda) - \rho_s L_s(\lambda) \quad (1b)$$

where L_{w+} is water-leaving radiance just above the water surface, originating from subsurface upwelling radiance and altered by transmissivity of the sea-air interface. E_d is downwelling irradiance above the water surface. L_t is the radiance received by the sensor pointed at the water surface and collects L_{w+} and a fraction ρ_s of the sky radiance L_s. The symbol λ is used for wavelength. Dependence of the radiances and ρ_s on zenith and viewing angles is not explicit in Eqs. (1a) and (1b). We only consider the case where φ_v is identical for L_s and L_t, while θ_v of the two radiance quantities is mirrored in the horizontal plane, as drawn in Fig. 1.

The two largest challenges in shipborne reflectance measurements are to maintain optimal viewing geometry (Aas, 2010; Hooker & Morel, 2003) and to determine an accurate value of ρ_s under variable illumination and surface roughness conditions (Aas, 2010; Mobley, 1999; Ruddick et al., 2006). Should these problems be overcome, shipborne $R_{rs}(\lambda)$ could prove a highly valuable complement to remote sensing imagery, while also contributing hyperspectral monitoring under clear and clouded conditions. The Methods section provides a brief description of the method used to maintain an angle close to $\varphi_v = 135°$, compensating the azimuth angle of our spectroradiometers for ship course and sun position. The main topic of this study is to describe and validate a new approach to estimate the sky radiance reflectance ρ_s, particularly for relatively clear coastal waters for which no current solutions exist.

Existing approximations of ρ_s have been based on sea surface roughness (or wind speed as a proxy), sensor viewing geometry, and the direct and diffuse fractions of downwelling irradiance (Aas, 2010; Mobley, 1999). The values of ρ_s predicted from these models hold true in general but are often suboptimal for individual measurements taken under continuously changing conditions (wave and ship motion, illumination). Alternatively, assumptions can be made on the spectral shape of reflectance. Ruddick et al. (2006) showed that R_{rs} in the near-infrared (NIR) has a highly conserved shape in moderately to highly turbid waters caused by the dominant absorption properties of water. This information can be used to validate, or optimize, R_{rs} spectra in turbid waters. For clear waters where NIR L_{w+} is too weak to discern the similarity spectrum a solution has not yet been presented. Lacking a more appropriate method, we may default to $\rho_s = 0.0256$, the value of the Fresnel reflection coefficient for a flat sea under fully diffuse light. For clear-sky conditions, dependence of ρ_s on waves has been modeled on wind speed W ($m\ s^{-1}$) such as described in Ruddick et al. (2006), switching to the clear-sky case when $L_s(750)/E_d(750) < 0.05$:

$$\rho_w = 0.0256 + 0.00039W + 0.000034W^2. \quad (2)$$

Alternatively, in optically deep (clear) waters the so-called 'black pixel assumption' can be used to determine ρ_s. R_{rs} is assumed to approximate zero at wavebands where $a >> b_b$ so that Eq. (1a) and (1b) can be solved for ρ_s which assumes the value of $L_t(\lambda)/L_s(\lambda)$ in the 'black' channels. The zero-reflectance condition is only met in the NIR where absorption by water is high, and in the ultraviolet-to-blue spectrum in clear waters with high humic substances absorption (e.g. Berthon & Zibordi, 2010).

Coastal waters exhibit wide variability in backscattering intensity due to the presence of suspended minerals from river sources and shallow banks. Neither of the above approaches will be consistently valid in such waters. We present an alternative method to estimate ρ_s designed to work with hyperspectral radiometric measurements of both clear and turbid waters. The method is based on the observation that downwelling and reflected upward (ir)radiance contain a multitude of narrow spectral features that originate from gas absorption in the outer layers of the sun and the Earth atmosphere (Fig. 2A). R_{rs} is given shape by the inherent optical properties of the water, and the spectral pattern or 'fingerprint' of the downwelling light should therefore not be observed in R_{rs}. In field measurements, when an unsuitable value for ρ_s is applied to calculate R_{rs}, the atmospheric features can be recognized in R_{rs}. Reciprocally, we can optimize ρ_s so that the presence of the atmospheric features in R_{rs} is minimized. This method is detailed in this paper and referred to as the 'fingerprint' method.

Isolation of the atmospheric fingerprint from water-leaving radiance requires that their spectral signatures are distinct. To illustrate that this is a realistic expectation, absorption shapes of optically active substances are shown in Fig. 2B for comparison against the (ir)radiance spectra in Fig. 2A. The distinct absorption peaks from pigments (simulated from Baltic Sea spring bloom measurements) are dampened by the broad absorption features of water in the NIR and by colored dissolved organic matter (CDOM) in the ultraviolet (UV). In conditions of phytoplankton bloom we may expect pigment absorption and fluorescence features to mask the distinct fingerprint of the atmospheric absorption in the visible spectrum, where atmospheric absorption features are already less prominent. However, even in those situations we expect that UV and NIR channels can be used to distinguish the atmospheric influence in water-leaving radiance. This hypothesis is tested using radiance data simulated with the radiative transfer approximation software Hydrolight 5.0 (Sequoia Scientific Inc.,

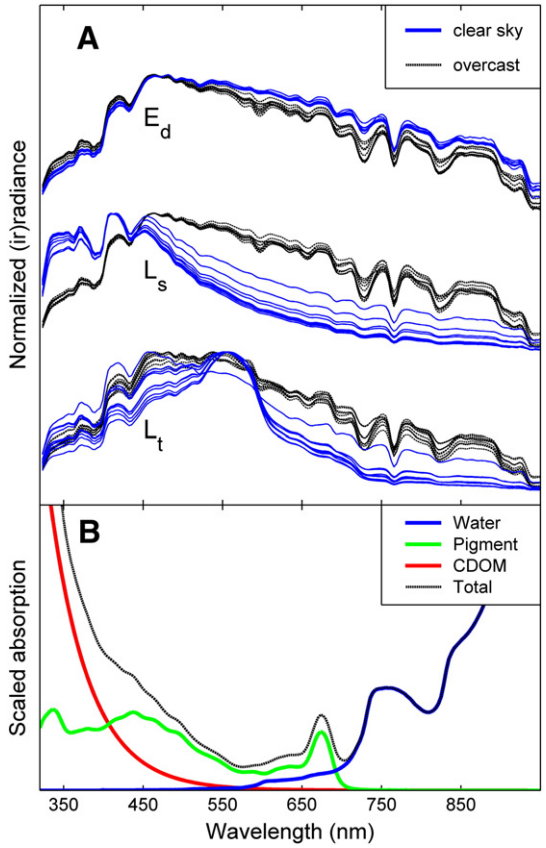

Fig. 2. (A) Field measurements illustrating the consistent presence of gas absorption features (valleys) in E_d, L_s, and L_t, in 20 randomly chosen samples under clear and overcast skies. All spectra are normalized to their maximum, and L_s and E_d plotted at an offset. These absorption features are distributed throughout the spectrum under overcast skies (black dashed lines). Blue features dominate under clear skies (blue lines). (B) Generic absorption spectra of water and main optically active constituents, CDOM and phytoplankton pigment, to illustrate that dampening by overlapping absorption signatures reduces distinct features in inherent optical properties, leaving many gas absorption features observed in panel A intact. The absorption spectra were resampled and smoothed from their original high-resolution measurements to mimic the spectral resolution of a TriOS RAMSES sensor.

WA, USA), and with a large data set of field observations from the Baltic Sea during spring and summer phytoplankton bloom.

2. Methods

2.1. Optimization of ρ_s

The optimization procedure for ρ_s takes place in three steps:

(1) identification of atmospheric absorption features that are present in both L_t and L_s,
(2) setting a high and a low limit for ρ_s and flagging suspect samples,
(3) a minimization function which yields optimized ρ_s and corresponding R_{rs}.

A detailed explanation of each step is given below. The algorithm was coded in Matlab 7 (The Mathworks) and tested with GNU Octave (v 3.4.3). A copy of this code is available from the authors.

(1) Illumination conditions and light absorption in the water column cause variability in the position and magnitude of peaks and valleys associated with gas absorption in the downwelling and reflected radiance. The different gas absorption features are therefore not equally prominent in all samples (Fig. 2). Consequently, L_t and L_s should be inspected pair-by-pair, identifying the most prominent features in each sample, for the best result in the optimization procedure. Only features which are detected in the same waveband in both L_t and L_s are selected.
The spectral locations of the most prominent features in a set of L_t and L_s spectra can be rapidly identified from the highest and lowest values in the first spectral derivative. The minima and maxima in the derivate correspond to the sharpest drops and rises in the spectra rather than the valley/peak positions, which does not influence algorithm performance. With increasing sensor spectral resolution, a gas absorption feature can be represented by more than one spectral channel. To avoid broad features from dominating the optimization we limit the band selection to the most prominent features within 10-nm intervals. The 750–780 nm range is omitted entirely to avoid the narrow and prominent oxygen absorption band. This band is so narrow that even slight differences between the spectral calibration of L_t and L_s sensors could dominate the optimization step, which would undo the advantage of getting a consensus solution of ρ_s based on multiple features spread out over the spectrum. If a single sensor is used to capture all (ir)radiance signals in sequence, the spectral calibration issue is not relevant but the risk of the single band dominating the optimization of ρ_s is still present.
(2) Upper and lower limits for ρ_s are used to speed up optimization and to catch suspect cases. We use the single-variable bounded nonlinear function minimization function *fminbnd* in Matlab 7 or GNU Octave, which takes lower and upper bounds as input. The lower limit for ρ_s is here set to 0.0240, which is just below the lowest value (0.0247) obtained with Hydrolight for a fully overcast sky, low (5 m s^{-1}) wind speed, and 45° solar zenith angle. Alternatives for the lower bound are the Fresnel reflectance of a flat sea surface for a given solar angle, or a wind-speed based value (Eq. 2). The upper limit is defined as the value of ρ_s that yields $R_{rs} = 0$ at any waveband in the 375–800 nm range. This limit value is equivalent to the 'black pixel' value, $L_t(\lambda)/L_s(\lambda)$. In waters where R_{rs} is expected to be zero or near-zero, the upper limit may be very close or equal to the true value of ρ_s and a margin can be added to prevent acceptable results from being flagged as suspect. Finally, cases where $L_t(\lambda)/L_s(\lambda) < 0.024$, i.e. where any value of ρ_s above the lower limit will yield negative R_{rs}, are a priori flagged as suspect.
(3) Optimization of ρ_s is carried out by evaluating the shape of $R_{rs}(\lambda_i)$ around every feature *i* selected in step 1. The best solution for ρ_s is expected when the shape of the downwelling radiance spectrum does not propagate to R_{rs}. This behavior is evaluated by fitting the area around each $R_{rs}(\lambda_i)$ (excluding the central waveband channel) to a second-order polynomial (*polyfit* function in Matlab or Octave). The fitted shape is noted $R^*_{rs}(\lambda_i)$. The bounded minimization function subsequently searches for the solution of ρ_s where the sum of absolute residuals of $R_{rs}(\lambda_i)$ from the polynomial fit $R^*_{rs}(\lambda_i)$ is smallest:

$$\text{minimize } f(\rho_s) = \sum_{i=1}^{n} \left| R_{rs}(\lambda_i) - R^*_{rs}(\lambda_i) \right| \quad (3)$$

where ρ_s is subject to the bounds defined in step 2, and the function $f(\rho_s)$ varies $R_{rs}(\lambda)$ through Eqs. (1a) and (1b).

Letting $R_{rs}(\lambda_i)$ approximate second-order polynomials implies that R_{rs} can be curved or sloped, but is forced to be smooth. Absorption features in the sky radiance have the opposite effect on the R_{rs} spectrum, and will therefore be minimized. Individual atmospheric absorption features may overlap with absorption peaks in water constituents that force R_{rs} in the same direction, but the consensus solution of ρ_s for multiple features spread out over the R_{rs} spectrum will unlikely suffer from such coincidences. It is important that the area over which the polynomial curve is fitted does not include multiple

features or local minima. As long as these conditions are met, the width of the area selected around each feature can be freely optimized, with a minimum of 5 consecutive channels to be able to fit the polynomial. Validation data in this study (details below) were obtained at 3.3-nm resolution *in situ* and at 2-nm resolution from radiative transfer simulations. For both data sets we used the narrowest possibility of 16.5-nm and 10-nm sections, respectively.

2.2. Simulated data sets

A data set of $L_t(\lambda)$, $L_s(\lambda)$, $E_d(\lambda)$, $R_{rs}(\lambda)$, and $\rho_s(\lambda)$ with $\theta_v = 40°$ and $\varphi_v = 135°$ was generated with Hydrolight to explore possible limitations of the ρ_s optimization technique. The atmospheric radiance simulations embedded in Hydrolight do not describe spectral variations with cloud cover increasing >40%. The model will yield identical spectral shapes for E_d and L_s under these clouded conditions. This is problematic when optimizing ρ_s since successive iterations of R_{rs} will experience very minor influences on the smoothness of R_{rs} within the gas absorption features, whereas the amplitude of the spectrum can still vary with changing ρ_s. The lower and upper limits of ρ_s are then reached before the algorithm converges on a solution. Because of this limitation we restricted all simulations to clear skies, where variations in ρ_s have a larger influence on R_{rs}. We used $\theta_s = 45°$, 80% relative humidity, ozone at 300 Dobson units, and the default marine aerosol model for all simulations. Upwelling radiances were simulated for wind speeds of 0, 5, 10, and 15 m s^{-1} and using parameterizations of the built-in 'new Case-1' as well as the 4-component Case-2 model for the optical properties of homogeneous, infinitely deep water columns. Case-1 (oceanic) waters were parameterized by chlorophyll *a* (Chl*a*) at concentrations 0.01, 0.1, 1, 10 and 50 mg m^{-3}. Anomalies in the default Chl*a*-specific absorption spectrum were removed. Case-2 waters were given Chl*a* concentrations of 1, 10, and 50 mg m^{-3} and suspended sediments (calcareous sand) were variable at 0, 5, 10, and 50 g m^{-3}. CDOM absorption was fixed at 0.2 m^{-1} at 443 nm with an exponentially declining spectral slope of 0.0176 nm^{-1}. Default settings for absorption of pure water and scattering by sea water were used. Up- and downwelling light fields were simulated for bands with a width and interval of 2-nm in the 300–900 nm range. Inelastic scattering was only included in the Case 1 water model. In total, 20 Case-1 and 48 Case-2 waters were simulated.

2.3. Field data

Field data were collected during three cruises with R/V *Aranda* on the Baltic Sea in 2010–2011. The cruises included the onset of the spring bloom of predominantly diatoms and dinoflagellates, and the start and end of summer blooms, when a large part of phytoplankton biomass consists of filamentous cyanobacteria. Cruises covered the Gulf of Finland, the Baltic Proper, and the Finnish Archipelago sea, including both clear and moderately turbid waters. The Baltic Sea is a brackish sea that suffers anthropogenic eutrophication and annual phytoplankton blooms. Exchange with the North Sea through the Kattegat is limited and the sea is consequently rich in (colored) dissolved organic matter. During the growth season, the particle population of the open sea is dominated by phytoplankton, reaching biomass in the order of 20–50 mg Chl*a* m^{-3} during the spring bloom and 5–15 mg Chl*a* m^{-3} during summer bloom. Outside bloom periods, the waters of the open Baltic Sea have low reflectance due to the combination of high dissolved matter absorption and low particulate scattering.

The spectroradiometers used to collect semi-continuous (15-s interval) shipborne E_d, L_s, and L_t were model RAMSES (TriOS Optical Sensors, Rastede, Germany), with 3.3-nm spectral resolution (0.3 nm accuracy). These sensors are typical of mid-range spectrometers used widely in coastal bio-optical and satellite product validation studies and have the advantage of a wide calibrated wavelength range (320–950 nm) which includes several atmospheric absorption features in the UV and NIR. A RAMSES-ACC with cosine collector was used to measure E_d in the proximity of the radiance sensors, away from objects that could obscure a free view of the sky. L_t and L_s were measured with RAMSES-ARC sensors with a 7° field-of-view (FOV) centered at nominal (excluding effects of wave motion) $\theta_v = 40°$ in upward (for L_s) and downward (L_t) directions. The radiance sensors were mounted on the axis of a stepper motor (0.9° step interval) to control φ_v within the unobscured view of the sea from the bow of R/V *Aranda*.

The stepper motor platform is used to compensate changes in the solar azimuth and ship course at regular (1-s) intervals, maintaining $\varphi_v = 135°$. For some combinations of ship course and sun azimuth, and depending on the mounting position of the sensors near the bow of the ship, neither clockwise nor counter-clockwise movement to $\varphi_v = 135°$ yields a free view of the sea. The sensors were then pointed as close to $\varphi_v = 135°$ as possible while remaining in the $\varphi_v = 90$–$135°$ interval, and the data were flagged as suboptimal. If $\varphi_v \geq 90°$ was not attainable, data were flagged as unusable for R_{rs}. The controller software continuously received GPS information (latitude, longitude, ship speed, course, UTC time) to calculate solar zenith and azimuth from longitude and UTC time, using equations given in Kirk (1994) based on solar declination as formulated by Spencer (1971). At low speed (<1 kn) GPS-based ship course is inaccurate. To continue collection of reflectance data during stationary periods the software can additionally parse NMEA phrases from a compass. Without a compass, the software pauses all measurements until the ship resumes its course at a speed >1 kn. The software to parse GPS data, calculate solar azimuth, send trigger signals to the stepper motor, trigger spectroradiometer readings, and receive and store data sent back by the RAMSES sensors, is available free of charge as code developed in Labview 2009 (National Instruments). The software can be obtained from the authors or through an online open source software archive (cf. Olsson & Simis, 2012).

Radiance data were recorded every day at 15-s intervals during 20 days at sea, mostly uninterrupted (e.g. for cleaning) during hours with $\theta_s \leq 60°$. The data set was subsequently filtered to meet three criteria, which resulted in 13,874 sets of (ir)radiance measurements:

(1) φ_v within 90–136°, to eliminate measurements obtained while the stepper-motor platform could not provide an unobstructed view of the sea. A slight margin (here 1°) from the optimal 135° was accepted to allow for the 1-second response time of the viewing angle adjusting mechanism, which is relevant when the ship changes course or rolls on waves.
(2) No underexposure, to avoid sensor integration times that are too short for the brightness of the target. The threshold was set at half of the dynamic range of the instrument at the peak of the spectrum (i.e. minimum raw signal > 2^{15} for the 16-bit resolution sensor).
(3) No oversaturation. Erroneously long integration times could cause signal saturation. For the RAMSES sensors used here, a peak raw signal >62000 counts was considered saturated.

The effect of illumination conditions (e.g. cloud cover) on the retrieval of ρ_s is evaluated with two indices to describe the downwelling radiance distribution. The first index is the ratio $\pi L_s(400)/E_d(400)$ which theoretically approximates the fraction of diffuse light in downwelling radiance. Because the L_s sensor measures a narrow solid angle (7° FOV), this index is expected to be sensitive to changing cloud cover. The second descriptor of illumination conditions is obtained from the quantum irradiance integrated over the photosynthetically active radiation (PAR) domain, $E_d(PAR)$. This $E_d(PAR)$ is compared to a simulated $E_d(PAR)$ for an ideal cloud-free sky. To obtain the latter we followed the model of Gregg and Carder (1990). GPS time and location and atmospheric pressure recorded by the ship weather station were used in the model. The ratio $E_d(PAR)$ over ideal-sky $E_d(PAR)$ suggests clear sky conditions when it is close to unity, while decreasing values suggest increasing cloud cover. Because the index depends on the irradiance measurement, it is expected to show less influence of rapidly changing cloud cover. We can therefore use the index to determine a

minimum light requirement for successful convergence of the spectral optimization technique for ρ_s.

Subsurface irradiance reflectance $R(0^-)$ spectra were collected alongside above-surface R_{rs} measurements at anchor stations, when weather conditions allowed. Two RAMSES-ACC sensors and a SeaBird 50 pressure sensor were mounted in a profiling cage to record depth profiles of $E_d(\lambda)$ and $E_u(\lambda)$, with the sun facing the deployment side of the ship. A reference $E_d(\lambda)$ sensor on deck was used to correct the subsurface signals for fluctuations in downwelling light. The three irradiance sensors were intercalibrated after every cruise, their irradiance spectra adjusted to the mean spectrum. $R(0^-)$ was calculated as the ratio of subsurface (zero-depth) E_u/E_d. To obtain the subsurface signals, measurements were extrapolated to zero depth using exponential curve fitting. Due to strong attenuation of NIR (absorption by water) and blue light (absorption by CDOM), $R(0^-,\lambda)$ data are limited to 350–800 nm. The vertical extrapolation method is sensitive to stratification of optically active constituents, particularly buoyant phytoplankton accumulated near the water surface. Measurements that were clearly affected were not used in comparisons with R_{rs} spectra. Only measurements for which at least 15 corresponding R_{rs} measurements were available were used for the validation exercise.

3. Results

3.1. R_{rs} retrieval accuracy with simulated data

Clear-sky Hydrolight simulations were used to evaluate the performance of ρ_s retrieval over a wide range of optical properties. Hydrolight includes effects of surface roughness through the wave statistics of Cox and Munk (1954a, 1954b) whereas (spectral) variability between the up- and downwelling radiances caused by broken cloud cover, ship movement, and whitecaps are not included. These generalizations limit the range of ρ_s that are simulated. For $\theta_s = 45°$, $\theta_v = 40°$, and $\varphi_v = 135°$ ρ_s is found between 0.0247 (5 m s^{-1} wind speed, 100% cloud cover) and 0.0375 (15 m s^{-1} wind, clear sky). For still wind conditions $\rho_s = 0.0257$ (regardless of cloud cover).

The varied optical configurations of the simulated water columns are illustrated in Fig. 3A with Hydrolight-simulated R_{rs} spectra corresponding to 5 m s^{-1} wind speed. Wind speed was a minor source of variation in simulated R_{rs} but the major source of variation in ρ_s. The optimization routine was run with extended lower and upper bounds for ρ_s (0 and 1, respectively), to better evaluate ρ_s retrieval performance. Only one extreme case-1 sample (Chl$a$ = 50 mg m^{-3}) converged to a solution whereas all other case-1 simulations reached the lower limit of ρ_s. The deviations in the resulting $R_{rs}(550)$ were nevertheless minor (Fig. 3B), which supports the understanding that the influence of reflected sky radiance on $R_{rs}(\lambda)$ was *a priori* limited in the simulations. In contrast, all 48 Case-2 samples resulted in convergence of ρ_s. Linear least-squares regression of the retrieved ρ_s values (observed) against the Hydrolight simulations (predicted) was $\rho_{s,obs} = 1.121 \times \rho_{s,pred} - 0.003$ ($n = 48$, $R^2 = 0.51$, root mean square deviation (RMSD) = 0.005). Comparison in terms of R_{rs} (Fig. 3B) yielded perfect correspondence at the green peak of $R_{rs}(550)$, with $R_{rs,obs}(550) = 0.988\ R_{rs,pred}(550) + 0.001$, $R^2 = 1.000$, RMSD = 0.0001.

3.2. Field data pre-processing

The high latitude of the Baltic Sea (all cruises departed from Helsinki at 60°N) resulted in relatively low sun elevation throughout the test period. The lowest (most favorable) θ_s were 34° and 50° in July and April, respectively. Initial filtering of the measurement set resulted in 13874 samples with φ_v in the 90–137° interval and excluding (rare) measurements with suboptimal sensor integration times. The position of the sensors on the bow of the ship allowed a large swath to adjust φ_v, so that 79% of the samples had $133 \geq \varphi_v \leq 136$.

The two indices for illumination conditions captured a wide range of variation during the validation cruises. Fig. 4A shows that the ratio $\pi L_s(400)/E_d(400)$ yielded high sample-to-sample variation (e.g. 23–24 and 29 July 2010, 14 July 2011), associated with broken and thin inhomogeneous cloud. Under such conditions, L_s measured in parallel with L_t is less likely to yield good representation of the sky radiance reflected on the water, particularly with increasing wave slopes. Short-term variability of the L_s/E_d ratio can thus be used to filter unstable illumination conditions from a dataset, as shown further below. The E_d(PAR) over ideal-sky E_d(PAR) ratio showed a much lower influence of rapidly changing cloud cover, as expected. On cloud-free days, when the ratio should be close to unity throughout

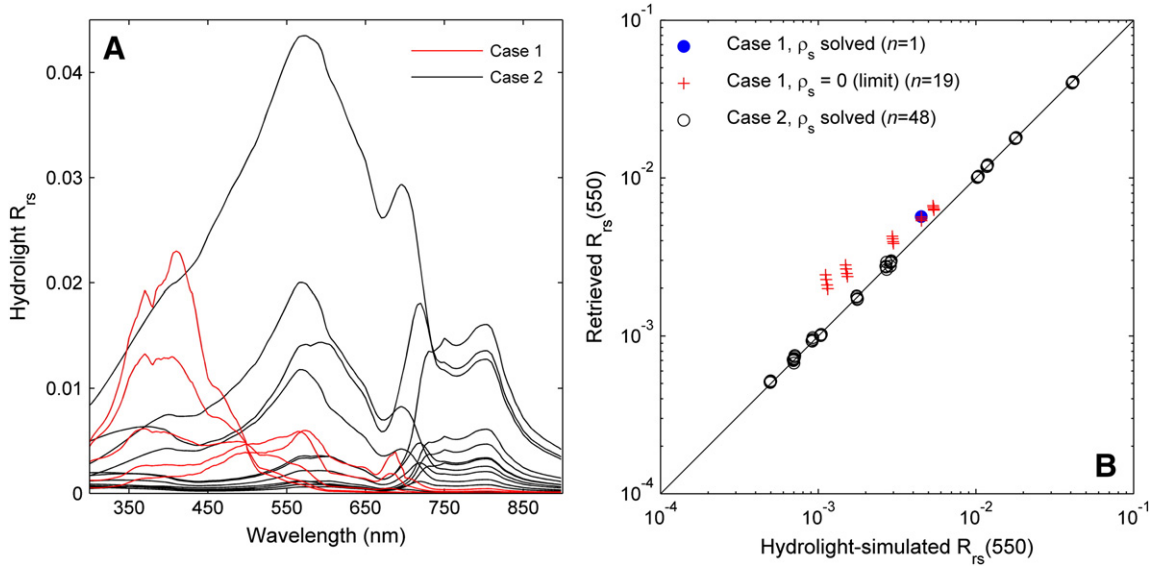

Fig. 3. (A) R_{rs} spectra generated with Hydrolight using Case 1 and Case 2 optical characterizations. Only spectra corresponding to wind speeds of 5 m s^{-1} are shown. (B) Retrieval results for $R_{rs}(550)$ from simulated radiances. Lower and upper limits for ρ_s were extended to 0 and 1, respectively, to fully assess algorithm limitations. From the Case-1 waters, only the sample with the highest Chl$a$ concentration converged to a solution (blue circles), in all other cases (red crosses) ρ_s reached the lower limit. All Case-2 water simulations (black circles) resulted in a solution ($R_{rs,obs}(550) = 0.99\ R_{rs,pred}(550) + 0.001$, $R^2 = 1.00$). Drawn black line marks unity.

the day, there was instead a tendency of E_d(PAR) to exceed the ideal-sky E_d(PAR) in the morning hours.

Wind speed and ship speed (Fig. 4B) were logged every 10 s. One storm event was included (day 4) with wind speed > 15 m s^{-1} during which the sensors likely experienced heavy spray, occasional splashing by breaking waves, and offsets to θ_v of at least 10°.

3.3. Retrieval success rate for ρ_s

Variations in cloud cover, solar angle, aerosol absorption, and optical properties of the water column are likely to influence the position and width of gas absorption features observed in E_d, L_t, and L_s. The procedure based on sorting peaks and drops in the derivative spectra yielded between 2 and 16 features in our data set, with average and standard deviation (SD) of 11.3 ± 2.9 features per set of radiance spectra. A histogram of the spectral location of these features (Fig. 5) shows that 10 spectral features were consistently found (present in >50% of all samples). These recurring spectral features were mostly from the ultraviolet (UV) and NIR range, where the downwelling (ir)radiance spectra are most heavily featured (Fig. 5, overlaid spectra) and the underlying R_{rs} shape is heavily dampened by absorption by CDOM and water.

Out of 13874 observations, the optimization technique converged on a value of ρ_s between the higher and lower limits in 3071 cases (22.1%). In 6495 cases (47%) the algorithm terminated at the higher limit to prevent negative R_{rs} in the 375–800 nm range. The lower limit of 0.0240 was reached in 3680 cases (26.5%). 628 cases (4.5%) were a priori flagged as suspect because any value of ρ_s above the lower limit would result in negative R_{rs}. We observed no effect of ship speed or position on these distributions.

The combination of relatively high-absorption, low-scattering waters of the open Baltic Sea may often result in near-zero R_{rs} in the NIR as well as in the UV (Berthon & Zibordi, 2010). Thus, a part of the ρ_s optimization results where the higher limit of ρ_s was reached may lie very close to the true value. Indeed, increasing the limit for ρ_s by 50% changed the number of optimized cases from 3071 (22.1%) to 7331 (52.8%). We maintain the stricter limit for ρ_s because a conclusive way to distinguish between realistic near-zero R_{rs} spectra and those resulting from poor measurement conditions was not established.

3.4. Relationships between ρ_s, illumination, and wind

Cloud cover is the largest source of variation in ρ_s and the range of optimized ρ_s values should consequently reflect the variability in illumination conditions during our field tests. Fig. 6A shows the separation of two ρ_s clusters from clear and clouded skies using the index $\pi L_s(400)/E_d(400)$. Clearer skies ($\pi L_s(400)/E_d(400) < 0.25$) resulted in average (±SD) sky radiance reflectance factors of 0.0467 ± 0.0148, notably higher than in the Hydrolight-simulated data set. Predominantly clouded skies ($\pi L_s(400)/E_d(400) > 0.8$) were associated with lower ρ_s values (0.0297 ± 0.0130). Only samples where ρ_s converged to a solution were considered in these distributions. We note that the selection criterion for clear skies used here ($\pi L_s(400)/E_d(400) < 0.25$) provides the same level of discrimination between clear and clouded cases as the ratio $L_s(750)/E_d(750)$, with an upper limit of 0.05 for clear skies, as formulated in Ruddick et al. (2006). Further nuances within the clear-sky cluster are visible when ρ_s is plotted against the E_d(PAR)/ideal-sky E_d(PAR) ratio (Fig. 6B). This index for illumination is insensitive to the distribution of cloud cover and highlights the considerable variability of ρ_s under well-lit but not necessarily cloud-free conditions, which appear to be found in the 0.5–1 range of this index.

The (frequent) cases where ρ_s reached the higher bound (to prevent negative R_{rs}) are plotted as dots in both panels of Fig. 6. The range of ρ_s was similar to that observed in cases of convergence of the method. This result suggests that Baltic Sea R_{rs} often approaches zero, but does not imply that these ρ_s values at the higher limit yield valid R_{rs} spectra.

No significant statistical relation was found between wind speed and retrieved ρ_s ($R^2 = 0.03$ and $R^2 = 0.01$ for clouded and clear-sky cases, respectively). These results clearly differ from previously reported modeled (Mobley, 1999) and experimental results (Toole et al., 2000, using $\varphi_v = 90°$, $\theta_v = 45°$). Long sensor integration times of the L_t sensor, in order to accommodate large θ_s, cloud cover, and low R_{rs}, could explain dampening of wind-wave effects. However, L_t sensor integration times were ≤ 1 s in over 90% of cases, too short to reduce wave effects at higher wind speeds and longer waves. No definitive explanation was found to explain the difference between our optimized ρ_s and those previously reported. However, we should bear in mind that optimizing ρ_s to yield well-behaved R_{rs} introduces the risk of propagating any error in the measurement into this single parameter, and can thus obscure the assumed

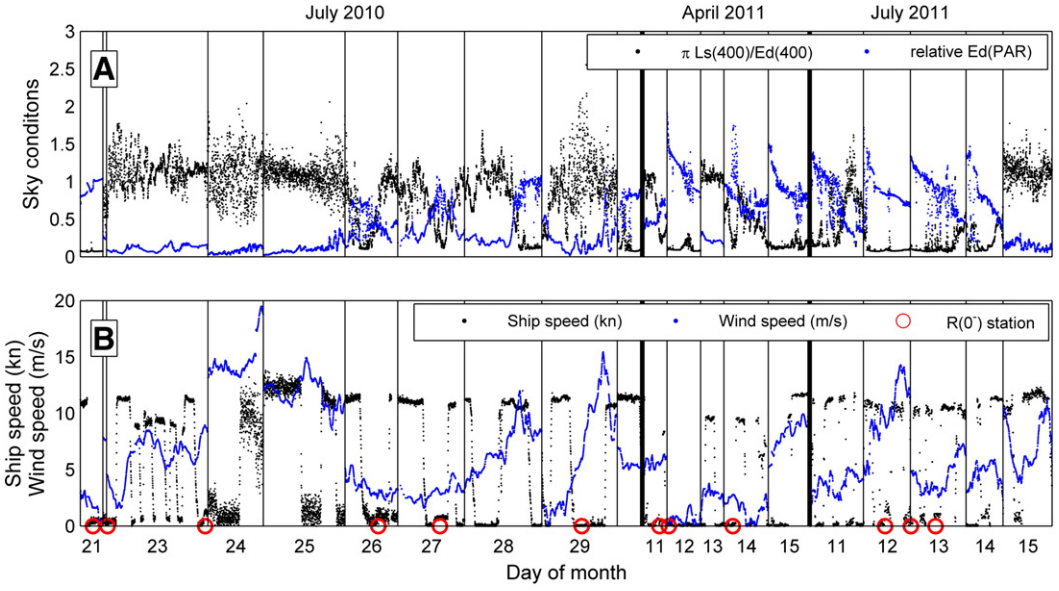

Fig. 4. Measurement conditions for the three cruises (20 days) during which field data was collected. (A) Sky conditions, expressed as (black markers) the ratio $\pi L_s(400)/E_d(400)$ and (blue markers) the PAR quantum irradiance E_d(PAR) relative to the idealized sky model of Gregg and Carder (1990). (B) Ship and wind speed. Sampling dates are indicated by months and day numbers at the top and bottom of the graph, respectively. The distribution of subsurface irradiance measurements used to validate the ρ_s retrieval is indicated by red markers in panel B and corresponds to the locations plotted in Fig. 7.

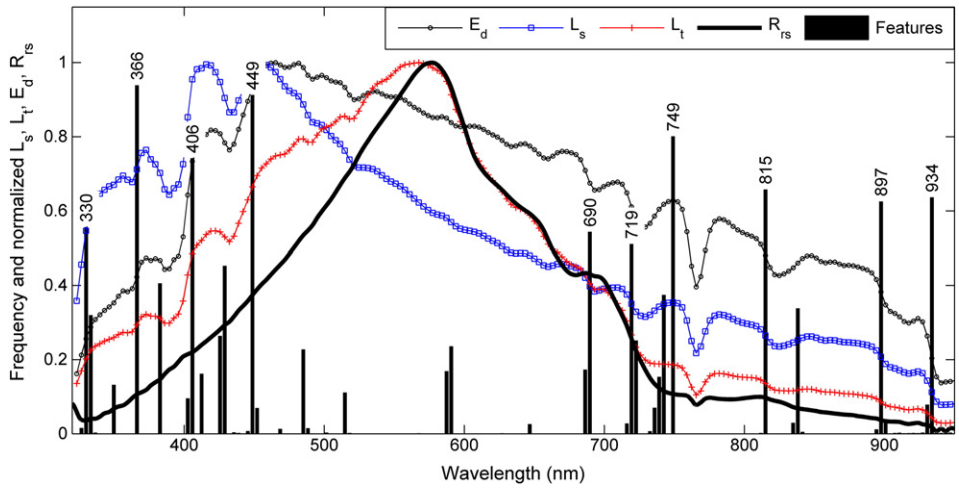

Fig. 5. Frequency of co-occurrence of spectral features in the first derivatives of L_s and L_t, based on 13874 simultaneous radiance measurements on the Baltic Sea. Spectral locations of the 10 most frequently recurring features are indicated with wavelength labels. The 750–780 nm region is excluded to prevent the narrow oxygen absorption band at 760 nm from dominating the optimization result. The histogram is overlaid on a set of (ir)radiance measurements taken on 11 April 2011, 12:02 GMT under a light cloud cover, and the corresponding R_{rs} spectrum with $\rho_s = 0.0489$ resulting from the fingerprint technique.

relation between ρ_s and waves. For studies dealing with separating these errors we refer to the work of Doxaran et al. (2004) and Toole et al. (2000).

3.5. Validation of R_{rs} retrieval at anchor stations

There is no 'ground truth' data to validate R_{rs} while the vessel is in motion. We can therefore only provide validation of the method against data collected at anchor stations, where we measured subsurface irradiance reflectance $R(0^-)$ by extrapolation to the surface of up- and downwelling irradiance profiles. The locations of these stations in the Baltic Sea are given in Fig. 7. Corresponding wind and illumination conditions can be read from Fig. 4. We avoid the translation between $R(0^-)$ and R_{rs}, with inherent uncertainties resulting from unknown air-sea interface effects or extrapolation errors, by comparing the spectra after normalization to their peak value in the 500–600 nm range. Results are plotted in Fig. 8 and photos illustrating illumination and wave conditions during the measurements are given in Fig. 9. The validation set contained a wide range of illumination conditions (E_d(PAR) = 74–1453 μmol photons m^{-2} s^{-1}, θ_s = 37–59°) and wind speeds ranging 0.4–9.2 m s^{-1}. Clear sky overhead was only experienced during stations (Figure panels) A and L. Station I was sampled in a mild fog. A summary of relevant measurement conditions is given above each panel of Fig. 8. The cloud cover index $\pi Ls(400)/E_d(400)$ is given as the average and standard deviation for the 20-min time window around the set of measurements. Combinations of bright illumination and low variability in illumination resulted in the best correspondence of R_{rs} and $R(0^-)$ and gave the highest number of R_{rs} based on optimized ρ_s (plotted in green). The correspondence of these R_{rs} spectra with $R(0^-)$ was in all cases an improvement over the R_{rs} generated with ρ_w (Eq. 2), which always underestimated sky radiance reflectance. High sun zenith angles and lower light intensity, particularly when coincident with weak reflectance (clearer water) reduced the number of observations where the spectral optimization succeeded. High variability in cloud cover during the measurements resulted in the poorest matches. For those R_{rs} results where ρ_s did not converge above its lower limit of 0.0240 (plotted in blue), correspondence was poorest.

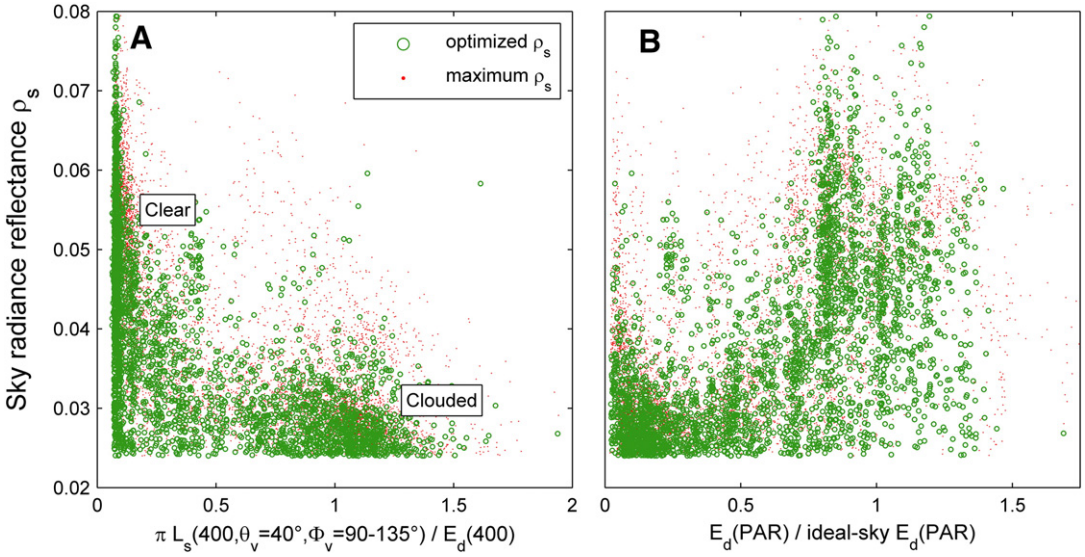

Fig. 6. Results of ρ_s retrieval versus (A) angularity of sky radiance expressed as $\pi Ls(400)/Ed(400)$, and (B) the fraction of E_d(PAR) relative to the ideal-sky model of Gregg and Carder (1990). Note that cases where ρ_s retrieval converged on a value between the higher and lower limits are emphasized in green (22% of all cases), while the more frequent (47%) cases where ρ_s reached the higher limit (allowing R_{rs} to be zero but not negative) are plotted as red dots.

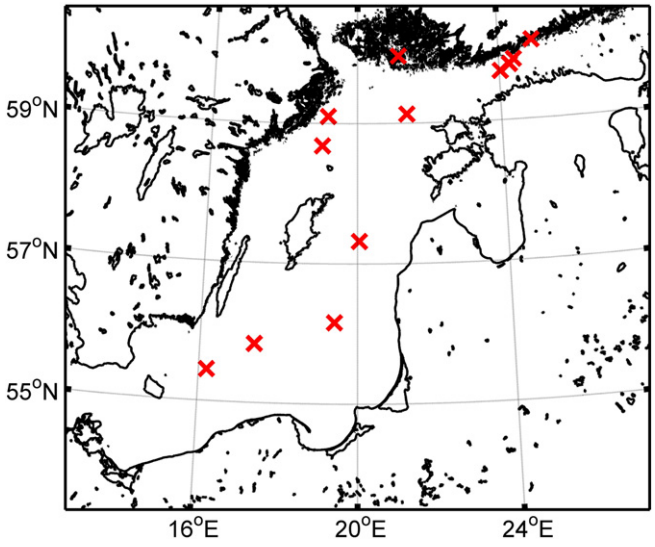

Fig. 7. Locations of Baltic Sea anchor stations where R_{rs} and $R(0^-)$ spectra were compared.

3.6. Data filtering based on illumination conditions

The preceding results illustrate that the variability in ρ_s and the retrieval success of the fingerprint optimization routine are determined by illumination conditions: cloud cover, the angularity of downwelling radiance, intensity of downwelling irradiance, and sun zenith angle. Assuming that the retrieval rate of ρ_s is a useful measure of R_{rs} product confidence, we can establish threshold values for acceptable stability and intensity of illumination in routine operation. In Fig. 10 we evaluate ρ_s yield in relation to the 20-minute variability in the two illumination indices used in this paper. The highest success rate (>50%) is experienced under lasting cloud-free conditions, when $\pi Ls(400)/E_d(400) < 0.25$ (Fig. 10A) with SD < 0.01 (Fig. 10B), or when the 20-minute average $E_d(PAR)$ exceeded the ideal-sky model $E_d(PAR)$ with a factor 1.1–1.2 (Fig. 10C). Outside these limits, the success rate of ρ_s retrieval rapidly drops to 20–30%, although retrieval rates up to 33% are still observed for $\pi Ls(400)/E_d(400) < 0.45$ with SD of <0.03 or for $E_d(PAR)$/ideal-sky $E_d(PAR) > 0.75$.

Optimization of ρ_s increasingly fails at the lower limit with decreasing intensity of downwelling irradiance, whereas the higher limit of ρ_s is more frequently met under well-lit conditions (Fig. 10C). The fraction of cases where ρ_s reached the lower limit (yielding the worst predictions of R_{rs}, see Fig. 8) increases sharply when $\pi Ls(400)/E_d(400) > 0.35$ and SD > 0.05 (Fig. 10A-B, respectively), with the average $E_d(PAR)$/ideal-sky $E_d(PAR) < 1$ and again when the latter drops to <0.65 (Fig. 10C). These conditions can be flagged as sub-standard, even when the cause for this behavior cannot be properly explained without more detailed observations of the sky radiance distribution and cloud cover.

4. Discussion

With the aim to collect automated, semi-continuous shipborne reflectance measurements, confidence in the quality of the product is more important than data density. A retrieval rate >20% of ρ_s with high confidence in corresponding R_{rs} is more than adequate for routine operation, particularly when combined with threshold limits to remove data collected under substandard measurement conditions. If we *a priori* reject unstable illumination conditions the success rate may rise to >50%. Because illumination conditions are the most important factor controlling the quality of R_{rs} retrieval, the success rate will be dependent on season and geographic location.

Efforts to control the viewing azimuth angle in an automated fashion constitute the foremost contribution to high-quality radiance measurements and increased spatial coverage. Mounted on the bow of the research vessel the unobstructed swath was close to 180° and azimuth angles between 90–135° and 133–137° were attained in 89% and 68% of measurements, respectively, while cruising at >1 kn. The spatio-temporal coverage of R_{rs} observations with minimized sun glint and reflected sky radiance can thus see substantial improvement from the use of static sensors on ships. Obviously, the use of moving parts requires due consideration. In the setup used here, a calibration routine for the viewing angle is implemented to verify at hourly intervals that the system functions properly.

Using three spectroradiometers, geolocation, and a known measurement geometry, no additional measurements are required to process the signals to R_{rs}. In addition, illumination indices can be calculated from the same measurements to inspect stability of the light field and establish data filtering based on irradiance thresholds. We thus arrive at an adequate system for implementation of above-surface reflectance measurements on ships of opportunity in coastal systems. A period of routine implementation would be beneficial to formulate more precise (regional) definitions of conditions in illumination, cloud cover stability, and solar elevation that support high-quality R_{rs} spectra.

We may expect that results improve further when conditions are less challenging than in the Baltic Sea test case. These challenges are (1) low reflectance caused by a high absorption over scattering ratio due to high CDOM absorption and a phytoplankton-dominated particle population. (2) Large θ_s experienced north of 55°N, and (3) placement of the sensors on the bow of the medium-sized (59 m) research vessel, 7 m from the water surface, and exposed to spray and ship heave. With increasing distance from the sensor to the water, the diameter of the observed sea area will increase proportionally to the sensor FOV, allowing both bright and dark slopes of multiple waves to be observed. Our sensor configuration (FOV = 7°, θ_v = 40°) mounted on the bridge of a large ferry would see an increase in the observed sea area in L_t from 3.8 m^2 (7 m height) to 43–110 m^2 (25–40 m height). Observations from taller ships should thus show less variability in reflected sky radiance between measurements. This in turn suggests that the variability between retrieved ρ_s of consecutive measurements could be used as a quality indicator.

Simulated radiance data did not provide conclusive support for the method due to the limited variability in the shape of $R_{rs}(\lambda)$ when varying ρ_s. In field data we observe a much wider variability but reference measurements are relatively scarce. Further validation of the automated processing scheme would therefore be a welcome effort, particularly in more turbid waters where the near infra-red similarity spectrum (Ruddick et al., 2006) can be used to compare and validate R_{rs} spectra. At the same time, the present algorithm appears to already provide significant improvement over the use of wind speed based correction for reflected sky radiance, which thus far has been the only available approach for clearer waters.

5. Conclusions

The presented method helps to overcome the final hurdle in obtaining sustained in situ R_{rs} data from moving vessels, which in turn can dramatically increase the available ground truth for satellite remote sensing as well as coverage of water quality estimates using hyperspectral close-range remote sensing. The use of a multitude of atmospheric absorption features to optimize ρ_s between realistic limits can be used to automatically remove measurements where L_t and L_s cannot be harmonized to yield non-negative R_{rs} without signs of the atmospheric absorption fingerprint. This satisfies two criteria for automated reflectance measurement processing; first, there is no need for expert interpretation of the measurements, and second, no supporting measurements are required. Illumination indices (cloud cover, light field stability, and intensity of downwelling irradiance) calculated from the same radiometric measurements can be used to predict suboptimal measurement conditions. Other requirements to optimize the quality of the reflectance measurement must still be met. The most important of these are to optimize the viewing

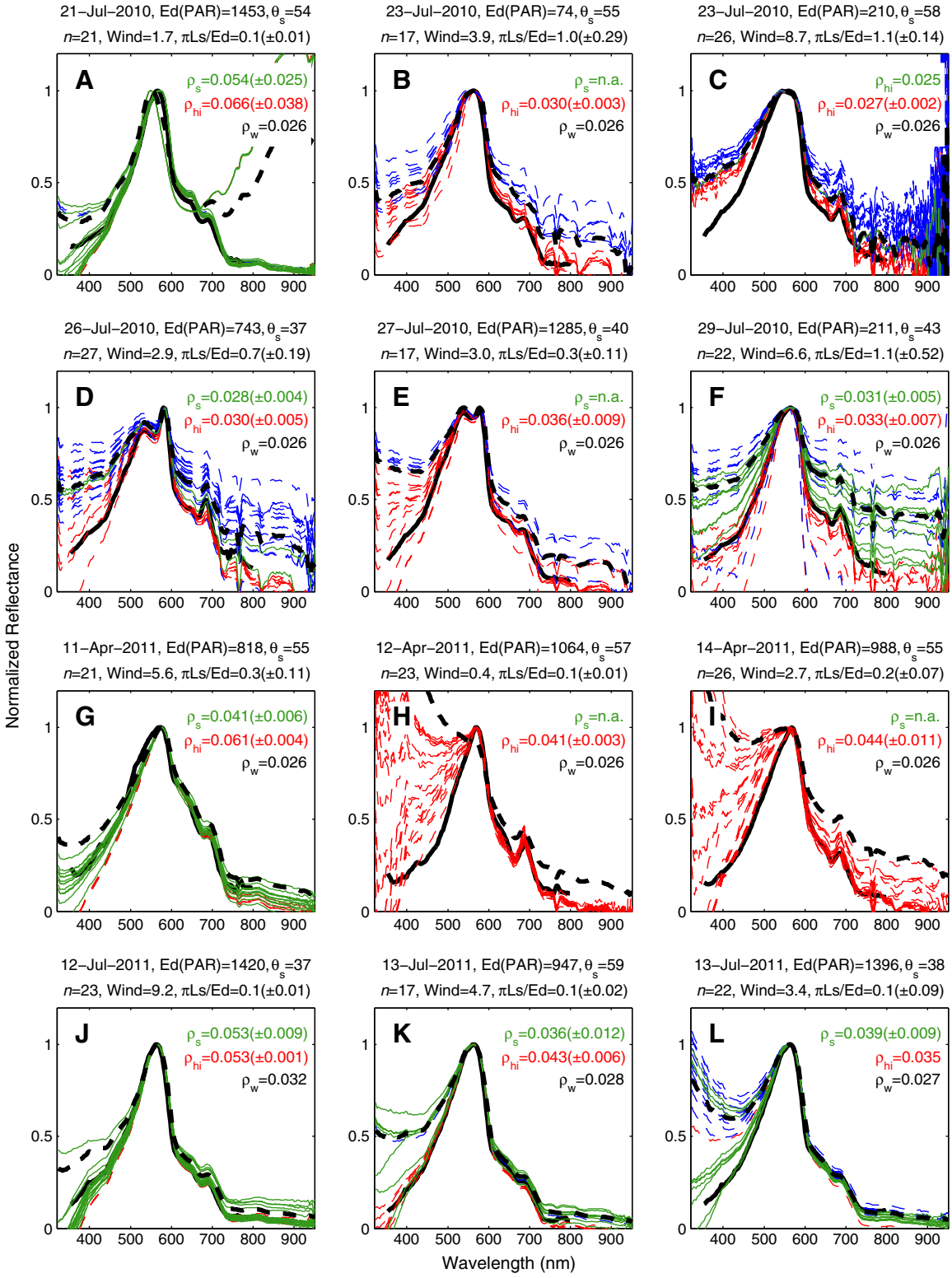

Fig. 8. Comparison of R_{rs} and $R(0^-)$ at anchor stations (locations in Fig. 7). All spectra are normalized to their values at the green peak. R_{rs} spectra plotted in green represent cases where ρ_s converged to a solution, average and standard deviation are given. Red curves and ρ_{hi} mark cases where the higher limit ($R_{rs} = 0$) was reached, blue curves indicate cases reaching the lower limit in optimization ($\rho_s = 0.024$). Thick drawn curves are the $R(0^-)$ observations, dashed curves are the average of R_{rs} spectra when based on wind speed (ρ_w, Eq. 2). Date, $E_d(PAR)$ in μmol photons m^{-2} s^{-1}, solar zenith angle θ_s in degrees, number of R_{rs} measurements (n), wind speed in m s^{-1}, and the mean and standard deviation of $\pi L_s(400)/E_d(400)$ in a 20-minute time window around the measurements are given above each panel. Photos illustrating illumination, visibility, and wave conditions during the measurements are given in Fig. 9.

azimuth angle, which can be achieved with minimal technical effort and at a fraction of the cost of placing additional static angle sensors on the same platform. Further, frequent intercalibration and occasional cleaning of the sensors must be maintained, as the present method relies on a valid spectral calibration between the sensors in a single system.

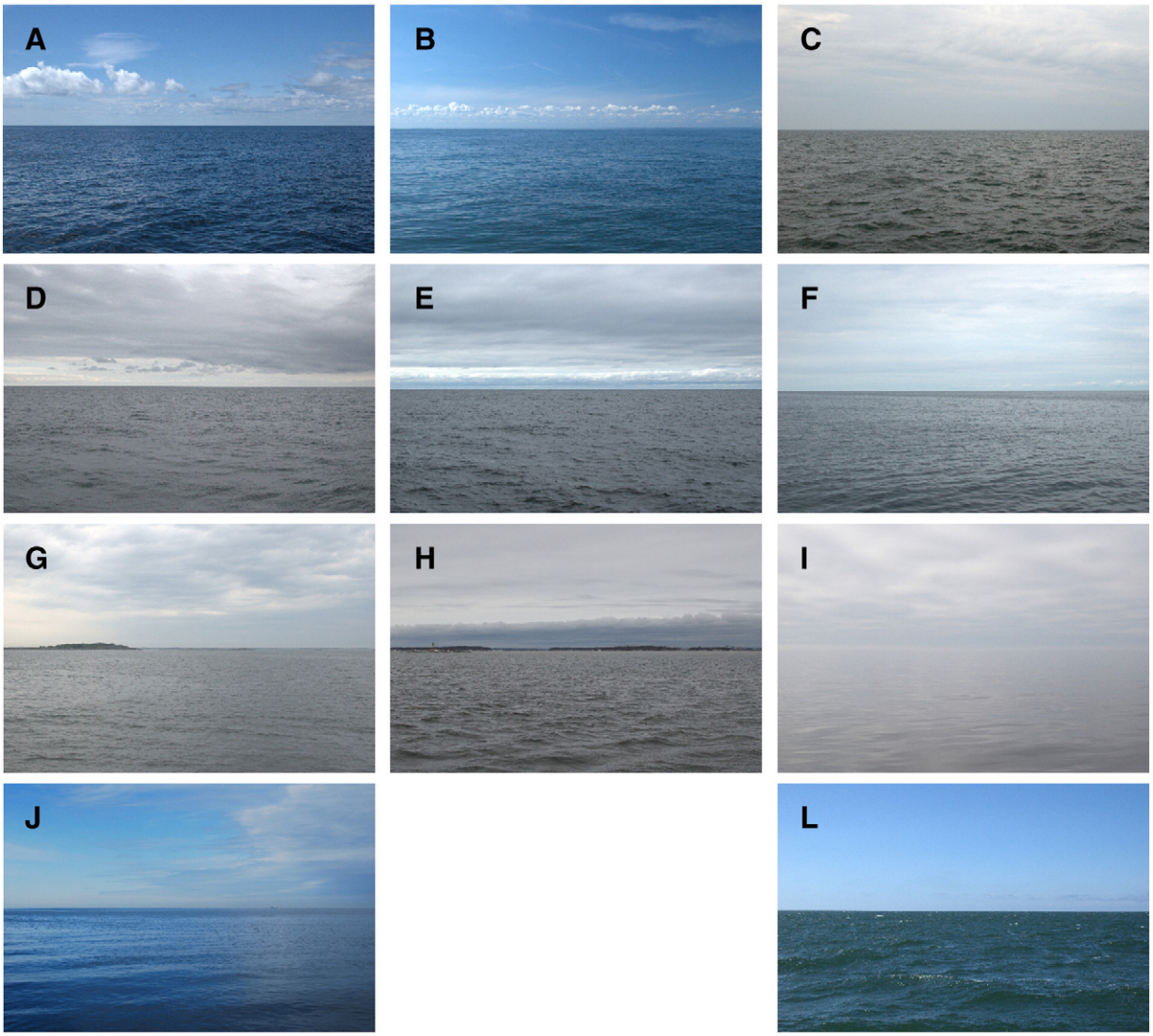

Fig. 9. Photos taken in the direction $\theta_v = 90°$ and $\varphi_v = 90–135°$ show cloud and wave conditions during the anchor stations used for validation of R_{rs} against $R(0^-)$ in Fig. 8 (corresponding panel order). Panel K is blank because no photo was taken.

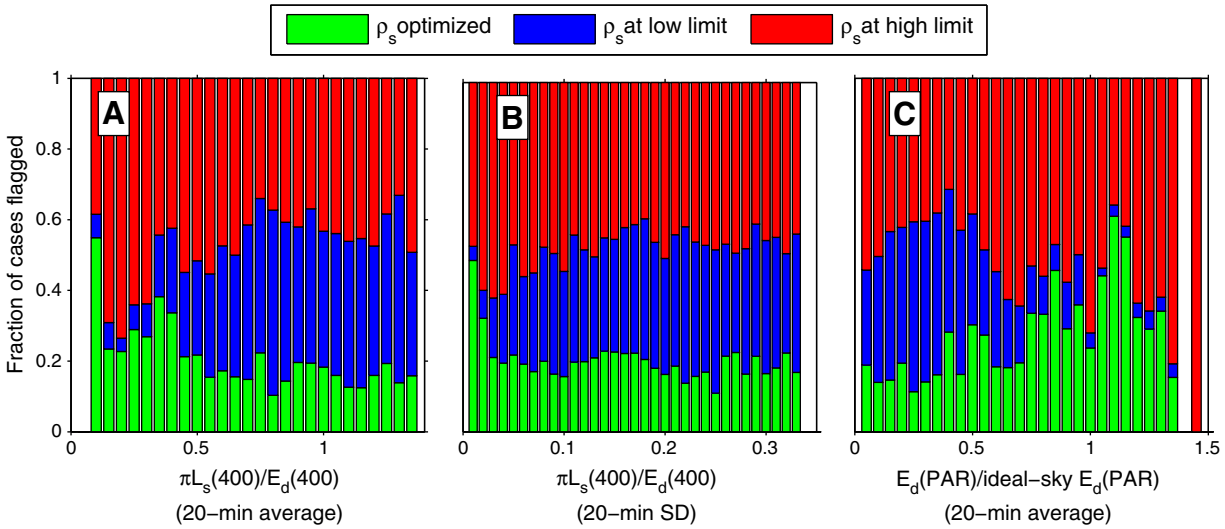

Fig. 10. Retrieval success of ρ_s in relation to the stability and intensity of downwelling light. In panels A–B the index of diffuse downwelling radiance $\pi L_s(400)/E_d(400)$ is used with the 20-min average (A) and standard deviation (SD, panel B). Panel C gives the 20-min average for the intensity of downwelling PAR irradiance relative to the ideal-sky model of Gregg and Carder (1990). Both indices indicate that a ρ_s retrieval rate exceeding 50% can be expected under stable clear-sky conditions. A success rate of approximately 20% may be expected under all other conditions, improving to approximately 30% as the intensity of downwelling irradiance exceeds 70% of the ideal-sky model (panel C). All plotted intervals (bars) contain at least 50 observations.

Acknowledgments

The authors wish to thank Hannu Vuori and Jari Pitkänen of the Marine Technology Services at the Finnish Meteorological Institute (FMI) for their excellent work constructing the stepper motor platform for the sensors. This research was financially supported through projects PROTOOL, a collaborative project (Grant 226880) co-funded by the Research DG of the European Commission (EC) within the RTD activities of the FP7 Thematic Priority Environment, and EC/IAPP project WaterS (Grant 251527). Time spent on this work by SGHS while visiting Water Insight BV (The Netherlands) within the WaterS project, and in particular inspiring discussions with Hans van der Woerd and Steef Peters during this time, are gratefully acknowledged.

References

Aas, E. (2010). Estimates of radiance reflected towards the zenith at the surface of the sea. *Ocean Science*, *6*, 861–876.

Behrenfeld, M. J., & Falkowski, P. G. (1997). Photosynthetic rates derived from satellite-based chlorophyll concentration. *Limnology and Oceanography*, *42*, 1–20.

Berthon, J. F., & Zibordi, G. (2010). Optically black waters in the northern Baltic Sea. *Geophysical Research Letters*, *37*, L09605.

Cox, C., & Munk, W. (1954a). Measurement of the roughness of the sea surface from photographs of the sun's glitter. *Journal of the Optical Society of America*, *44*, 838–850.

Cox, C., & Munk, W. (1954b). Statistics of the sea surface derived from sun glitter. *Journal of Marine Research*, *13*, 198–227.

Doxaran, D., Cherukuru, R. C. N., & Lavender, S. (2004). Estimation of surface reflection effects on upwelling radiance field measurements in turbid waters. *Journal of Optics A: Pure and Applied Optics*, *6*, 690–697.

Falkowski, P. G., Barber, R. T., & Smetacek, V. (1998). Biogeochemical controls and feedbacks on ocean primary production. *Science*, *281*, 200–206.

Gordon, H. R., Brown, O. B., & Jacobs, M. M. (1975). Computed relationships between the inherent and apparent optical properties of a flat homogeneous ocean. *Applied Optics*, *14*, 417–427.

Gregg, W. W., & Carder, K. L. (1990). A simple spectral solar irradiance model for cloudless maritime atmospheres. *Limnology and Oceanography*, *35*, 1657–1675.

Hooker, S. B., & Morel, A. (2003). Platform and environmental effects on above-water determinations of water-leaving radiances. *Journal of Atmospheric and Oceanic Technology*, *20*, 187–205.

Kirk, J. T. O. (1994). *Light and photosynthesis in aquatic ecosystems.* : Cambridge University Press.

Mobley, C. D. (1999). Estimation of the remote-sensing reflectance from above-surface measurements. *Applied Optics*, *38*, 7442–7455.

Morel, A. (1980). In-water and remote measurement of ocean color. *Boundary-Layer Meteorology*, *18*, 177–201.

Mueller, J. L., Morel, A., Frouin, R., Davis, C., Arnone, R. A., Carder, K. L., et al. (2003). Radiometric measurements and data analysis protocols. In J. L. Mueller, G. S. Fargion, & C. R. McClain (Eds.), *Ocean optics protocols for satellite ocean color sensor validation*. Greenbelt, Maryland: NASA.

Olsson, J., & Simis, S. G. H. (2012). RFlex: Spectroradiometer control for shipborne reflectance measurements. http://sourceforge.net/projects/rflex/

Preisendorfer, R. W. (1976). *Hydrologic optics*, *Vol. 1*, : U. S. Department of Commerce.

Ruddick, K., De Cauwer, V., & Park, Y. -J. (2006). Seaborne measurements of near infrared water-leaving reflectance: The similarity spectrum for turbid waters. *Limnology and Oceanography*, *51*, 1167–1179.

Spencer, J. W. (1971). Fourier series representation of the position of the sun. *Search*, *2*, 172.

Toole, D. A., Siegel, D. A., Menzies, D. W., Neumann, M. J., & Smith, R. C. (2000). Remote-sensing reflectance determinations in the coastal ocean environment: Impact of instrumental characteristics and environmental variability. *Applied Optics*, *39*, 456–469.

Tyler, J. E. (1960). Radiance distribution as a function of depth in an underwater environment. *Bulletin of the Scripps Institution of Oceanography*, *7*, 363–411.

Zibordi, G., Berthon, J. F., Melin, F., D'Alimonte, D., & Kaitala, S. (2009). Validation of satellite ocean color primary products at optically complex coastal sites: Northern Adriatic Sea, Northern Baltic Proper and Gulf of Finland. *Remote Sensing of Environment*, *113*, 2574–2591.

Zibordi, G., Strombeck, N., Melin, F., & Berthon, J. F. (2006). Tower-based radiometric observations at a coastal site in the Baltic Proper. *Estuarine, Coastal and Shelf Science*, *69*, 649–654.